Title
A numerical study of dynamo action as a function of spherical shell geometry

Journal
Earth and Planetary Science Letters, 236(1-2)

ISSN
0012-821X

Authors
Heimpel, MH
Aurnou, JM
Al-Shamali, FM
et al.

Publication Date
2005-07-01

DOI
10.1016/j.epsl.2005.04.032

Peer reviewed

Available online at www.sciencedirect.com
SCIENCE DIRECT®
ELSEVIER
Earth and Planetary Science Letters 236 (2005) 542–557
EPSL
www.elsevier.com/locate/epsl

A numerical study of dynamo action as a function of spherical shell geometry

M.H. Heimpel[a,*], J.M. Aurnou[b], F.M. Al-Shamali[a,1], N. Gomez Perez[a]

[a]*Department of Physics, University of Alberta, Edmonton, Alberta, Canada T6G 2J1*
[b]*Department of Earth and Space Sciences, University of California, Los Angeles, 90095-1567, USA*

Received 20 September 2004; received in revised form 24 February 2005; accepted 8 April 2005
Available online 17 June 2005
Editor: S. King

Abstract

The geometry of the liquid region of a planetary core can effect core convection and magnetic field generation processes. Varying the spherical shell radius ratio, $\chi = r_i/r_o$, illustrates differences between planets with differing core radius ratios as well as how dynamo processes vary with time in an evolving planetary core. Here we study numerical models of thermally driven dynamo action in a rotating shell of outer radius r_o with electrically conducting Boussinesq fluid that surrounds an equally conductive solid inner sphere of radius r_i. Dynamo solutions are found for $0.15 \leq \chi \leq 0.65$ at Ekman number $E = 3 \times 10^{-4}$, Prandtl number $Pr = 1$, and magnetic Prandtl number $Pm = 5$, with mechanically rigid, isothermal boundary conditions. In cases with mildly supercritical Rayleigh numbers, Ra, convection occurs in the form of columnar plumes aligned with the rotation axis. In thick-shelled cases ($\chi = 0.15$), onset of axial dipolar dynamo action occurs at relatively high Ra by the action of a single turbulent columnar plume. In thinner shells ($\chi \geq 0.25$), multi-plume columnar convection generates strongly dipolar dynamo fields near the onset of convection. Although some of our control parameters are far from planetary values, the outer boundary Elsasser number, Λ, (a non-dimensional measure of magnetic field strength) for thinner shell cases is comparable to that for the Earth's core–mantle boundary and estimates for the dynamos of Jupiter and Saturn. In contrast, thick shell, single plume dynamos produce relatively low Elsasser numbers at the outer shell boundary, possibly relevant to the magnetic field of Mercury. For a single evolving planet, these results imply that a transition during early inner core growth from a single plume or regional convective regime to a multi-plume or global convective regime could produce a significant increase in the exterior global magnetic field intensity. Our calculations are consistent with observations of axial dipole dominated planetary magnetic fields and support the concept of a geocentric axial dipolar field for much of Earth's history.

Keywords: core convection; geodynamo; planetary magnetic fields; inner core

* Corresponding author. Tel.: +1 780 492 3519; fax: +1 780 492 0714.
E-mail address: mheimpel@phys.ualberta.ca (M.H. Heimpel).
[1] Present address: Department of Physics, Athabasca University, Athabasca, AB, Canada.

0012-821X/$ - see front matter © 2005 Elsevier B.V. All rights reserved.
doi:10.1016/j.epsl.2005.04.032

1. Introduction

Recent satellite observations have expanded the number of planets in the solar system known to have intrinsic magnetic fields (e.g., [1]). Self-sustained, dipole-dominant dynamos are likely to exist in the cores of Earth, Jupiter, Saturn, Ganymede and perhaps Mercury [2]. For these planets, the dipole axis appears to be aligned within approximately 10° of the planetary rotation axis. In contrast, fly-by data from the Voyager II mission has shown that Neptune and Uranus have dynamos that feature strong non-dipole magnetic field components and a dipole component that is inclined away from the rotation axis [3]. Further satellite measurements suggest that ancient dynamos existed on the moon and Mars [4]. These observations raise the question as to how the style and efficiency of dynamo generation varies with evolving core geometry.

The radius ratio, $\chi = r_i/r_o$, where r_i and r_o are the inner and outer core radii, respectively, is known precisely for the Earth's core: $\chi = 1220\ \text{km}/3485\ \text{km} \simeq 0.35$. However, at the present time, outer core radii of other planetary bodies must be estimated via indirect geophysical modeling, and inner core radii prove difficult to constrain [5,6]. Thus, core radius ratio values are not known for any other planets, and may vary greatly for different bodies. In this study we carry out a systematic parameter study of the effects of low to moderately high spherical shell radius ratio, $0.15 \leq \chi \leq 0.65$, to investigate how spherical shell geometry can affect thermally driven magnetic field generation.

Most numerical studies of dynamo action have focused on understanding the magnetic field of the Earth. In such models, the main features of the Earth's magnetic field can be reproduced, even though the models suffer from severe resolution limitations [43]. Nearly axial, columnar convection produces high latitude flux patches that sum together to produce a strong dipolar field at the outer shell boundary [8,9]. These studies show that, in models with strongly columnar convection, the magnetic field is produced by an α^2-dynamo mechanism in which large-scale helical motions associated with the convection columns generate the poloidal field from the toroidal field as well as the toroidal field from the poloidal field [10]. In models run at a greater degree of convective supercriticality, strong azimuthal flows develop that generate relatively strong toroidal fields from poloidal fields via the so-called ω-effect. These models may be classified as either αω- or $\alpha^2\omega$-dynamos [7,11].

The mode of thermal evolution of the Earth's core places strong constraints on inner core growth and on the generation of buoyancy, which drives the geodynamo. There has been considerable recent interest in estimates of the age of the inner core, which range from roughly 1 to 4 billion yr [12–16]. Two major sources of buoyancy production at the inner core boundary (ICB) are thought to be latent heating and compositional buoyancy. The latter is due to the exclusion of volatile elements, such as S or O, from the inner core during solidification from the iron alloy outer core. Buoyancy can be produced at the core mantle boundary (CMB) via either secular cooling or internal heating, which can come from long-lived radiogenic isotopes, perhaps of ^{40}K, within the core [14–16].

The relative importance of heat sources driving convection changes with time and inner core growth. Secular cooling and internal heating would be responsible for driving core convection prior to inner core nucleation. As the inner core grows, buoyancy production due to composition and latent heating increases. Although internal heating is thought to be the largest source of heat flux out of the core, it is likely a minor source of the buoyancy that drives convection, compared to compositional buoyancy production at the ICB [13,16–18]. Nor does internal heating necessarily drive convection near the CMB. Depending on the radial density profile, heat transfer may occur via conduction across the CMB if the thermal gradient there is subadiabatic. In the thermal evolution model of Buffett et al. [17], the efficiency of both thermal and compositional convection increases as the inner core grows, with thermal convection processes dominating early on. However, when the inner core radius becomes greater than about 240 km, which corresponds to a radius ratio $\chi \approx 0.07$, compositional convection becomes more efficient than thermal convection. This implies that buoyancy production responsible for driving the geodynamo has been concentrated near the ICB for much of the growth of the inner core.

Recent studies have begun to simulate behavior of dynamos using various geometries that are applicable to cases other than the present-day Earth. Drew [19] and Morrison and Fearn [20] have studied dynamo action in a 2.5D dynamo model where the outer core radius and the planetary rotation rate are held constant while the radius ratio varies. In particular, Morrison and Fearn [20] investigate the range $0.025 \leq \chi \leq 0.5$. For a fixed outer boundary heat flux they find that dynamo action is strongest for $\chi = 0.25$ but ceases close to $\chi = 0.5$ as convection weakens due to thinning of the fluid shell. They also find smaller radius ratio cases to be more stable in time compared to thinner shelled cases and that their solutions can be strongly sensitive to the initial conditions.

Roberts and Glatzmaier [21] have carried out 3D geodynamo simulations using three different radius ratio values. Each case is subject to a different thermo-compositional forcing strength, estimated to approximate Earth's core conditions at early, present and late stages of core evolution. In their study these three cases correspond to $\chi = 0.0875$, 0.35 and 0.70, respectively. Similar to Morrison and Fearn [20], they find that the field is strongly dipolar and relatively steady in time for the $\chi = 0.0875$ case. In contrast, the high radius ratio case features a more time-dependent field with quadrupole and octopole terms that are closer in amplitude to the still dominant dipole component.

Sakuraba and Kono [22] have numerically studied internally heated dynamos with and without an inner core. The case with an inner core is for an earth-like geometry. They find that the two models produced comparable, axially dipolar magnetic fields. The main difference is that the case with an inner core produces a more stable field than the case without an inner core.

Schubert and Zhang [23] have carried out kinematic dynamo calculations in which they vary both the spherical shell radius ratio and the conductivity ratio between the shell fluid and the solid conductor within the inner shell. They find for $\chi \lesssim 0.5$ that steady kinematic dynamo action is only negligibly affected by the inner core conductivity and volume. In contrast, oscillatory solutions occur for cases in which $\chi \gtrsim 0.5$ and the electrical conductivity of the inner core is less than 5 times that of the surrounding fluid.

In addition to the studies, outlined above, that produce axial dipole fields, cases have been found in which the field is inclined away from the axis of rotation of the shell. In simulations of weakly supercritical convection, Ishihara and Kida [24] find a dipolar magnetic field may be generated with its dipole axis lying in the equatorial plane. Aubert and Wicht [25] have carried out a systematic parameter study and find equatorial dynamos in the range $0.45 \leq \chi \leq 0.70$ for cases with Rayleigh numbers between 1.1 and 1.5 Ra_c, in agreement with Ishihara and Kida's findings.

Even more complex fields have been produced in previous numerical dynamo models. Grote and Busse [26–28] find quadrupolar and oscillatory hemispherical dynamos for cases with stress-free, isothermal, electrically insulating boundary conditions with partial internal heating. Stanley and Bloxham [29] produced high radius ratio, non-axial dynamo models with strong quadrupole and octopole terms. Their highly supercritical models make use of stress-free boundary conditions, hyperdiffusion, and a stably stratified, conducting fluid inner core region. The precise mechanisms that produce these complex field morphologies are not well understood at present.

Here we expand upon previous work on rotating thermal convection in a self-gravitating shell over the radius ratio range $0.10 \leq \chi \leq 0.92$ [30]. In that study, non-magnetic rotating convection calculations were made at Ekman numbers of 10^{-3}, 3×10^{-4} and 10^{-4}, with the Prandtl number held fixed at unity. We found that the variation of the critical Rayleigh number for the onset of convection, Ra_c, could be described by a single, separable function of Ekman number and radius ratio. In this paper, we model dynamo action in an electrically conducting Boussinesq fluid as a function of spherical shell radius ratio. In Section 2 we discuss the governing equations, boundary conditions and numerical methods; Section 3 contains the results of the numerical simulations; discussion of the results is presented in Section 4; the findings are summarized in Section 5.

2. Theory and model

2.1. Governing equations

The governing equations for time-dependent, three-dimensional, rotating thermal convection of

an electrically conducting Boussinesq fluid are given by

$$E\left(\frac{\partial \mathbf{u}}{\partial t}+\mathbf{u}\cdot\nabla\mathbf{u}-\nabla^2\mathbf{u}\right) = -\nabla P-2\hat{z}\times\mathbf{u}+\frac{RaE}{Pr}\frac{g(r)}{g_o}\hat{r}T+\frac{1}{Pm}(\nabla\times\mathbf{B})\times\mathbf{B} \quad (1)$$

$$\frac{\partial \mathbf{B}}{\partial t} = \nabla\times(\mathbf{u}\times\mathbf{B})+\frac{1}{Pm}\nabla^2\mathbf{B} \quad (2)$$

$$\frac{\partial T}{\partial t}+\mathbf{u}\cdot\nabla T=\frac{1}{Pr}\nabla^2 T \quad (3)$$

$$\nabla\cdot(\mathbf{u},\mathbf{B})=0 \quad (4)$$

These equations are solved simultaneously to determine the temperature field T, pressure field P, the fluid velocity vector $\mathbf{u}$ and the magnetic field vector $\mathbf{B}$. The inner and outer spherical boundaries are isothermal with a temperature difference ΔT maintained across the shell. No-slip boundary conditions are employed and both boundaries are co-rotating at angular velocity $\Omega\hat{z}$. The solid region contained within r_i, which represents a planet's solid inner core, is assigned the same electrical conductivity as the surrounding fluid. The region exterior to r_o, which corresponds to a planetary mantle, is electrically insulating. The strength of gravity $g(r)$ varies linearly with radius, with $g_o=g(r_o)$. The thermal expansion coefficient α, kinematic viscosity ν, thermal diffusivity K, magnetic diffusivity η, and planetary rotation rate are Ω all held constant.

The equations have been non-dimensionalized using the following scales: the viscous diffusion timescale $\tau_\nu=D^2/\nu$ for time, fluid shell gap width $D=r_o-r_i$ for length, ν/D for velocity, $\rho\nu\Omega$ for pressure, ΔT for temperature and $\sqrt{\rho\mu_o\eta\Omega}$ for magnetic field where ρ is the fluid density and μ_o is the magnetic permeability. The resulting non-dimensional parameters are:

the Rayleigh number $$Ra=\frac{\alpha g_o \Delta T D^3}{\kappa\nu}, \quad (5)$$

the Ekman number $$E=\frac{\nu}{\Omega D^2}, \quad (6)$$

the Prandtl number $$Pr=\frac{\nu}{\kappa}, \quad (7)$$

the magnetic Prandtl number $$Pm=\frac{\nu}{\eta}, \quad (8)$$

the radius ratio $$\chi=\frac{r_i}{r_o}, \quad (9)$$

and the Elsasser number $$\Lambda=\frac{B^2}{\rho\mu_o\eta\Omega}. \quad (10)$$

The first five parameters are control inputs for each calculation. The Elsasser number, which is the ratio of the Lorentz to the Coriolis force, is an output parameter used in the analysis and discussion of the results.

In our calculations, the spherical shell gap width is fixed to $D=1$. For a fixed value of D, the radii of the inner and outer shells both increase with χ, as explained in detail in Al-Shamali et al. [30]. Using this parameterization, constant E results in constant non-dimensional strength of the rotational forces. In contrast, for a planet with fixed outer core radius and a growing inner core, the outer core shell thickness varies as $D=r_o(1-\chi)$. Thus, E does not remain constant but increases with χ such that $E=\nu/[\Omega r_o^2(1-\chi)^2]$ [20]. However, given that planetary core convection is in the asymptotic low E regime [31], even large changes in χ are not likely to dramatically change the style of convection. Thus, in our simulations, which are not made in the low E asymptotic regime, we define E in terms of D so that the strength of the Coriolis force does not vary with χ. Note also that we use the classical definition of the Rayleigh number: Ra is defined in Eq. (5) in terms of the fluid shell thickness, D, instead of the outer boundary radius, r_o. Later we will recast our results in terms of a second Rayleigh number defined in terms of r_o, which corresponds more closely to the case of a planet with a fixed core radius and a shrinking fluid shell gap width.

Latent heat production, compositional convection, and internal heating can be numerically modeled using constant temperature or heat flux boundary conditions and an additional non-dimensional source term S in the energy equation. The sign and relative strength of the source term can range from $S=-1$ for purely compositional convection to $S=+1$ for internal heating or secular cooling [32–34]. Purely compositional convection, driven by solidification of the inner core, has been modeled with $S=-1$, constant temperature inner boundaries, and zero heat flux at the outer

boundary [34]. For this set of conditions buoyancy is produced near the inner boundary, with no buoyancy production at the outer boundary. On the other hand, pure internal heating may be implemented with $S=1$, zero heat flux at the inner boundary and constant temperature at the outer boundary. This insures that buoyancy is produced preferentially near the outer boundary. We can compare these two end-member conditions for buoyancy production with the isothermal boundary heating case (implemented here) with $S=0$ and constant ΔT between the inner and outer boundaries. This results in buoyancy production at both boundaries. Thus, seen in terms of numerical modeling, boundary driven thermal convection lies dynamically between pure compositional convection and pure internal heat-driven convection. Considering the level of uncertainty of the relative contribution of buoyancy sources in the cores of the Earth and planets, this choice seems natural (albeit simple) for planetary dynamo modeling.

2.2. The numerical model

The spherical dynamo code used here was developed originally by G. Glatzmaier and has been modified by U. Christensen and J. Wicht [35–37]. We are presently using Wicht's version MagIC2.0 [37]. The numerical technique uses the spectral transform method to solve Eqs. (1)–(4) simultaneously. The fields are expanded in the radial direction using Chebyshev polynomials and in the latitudinal and longitudinal directions using spherical harmonics. The Ekman, Prandtl and magnetic Prandtl numbers are held fixed at $E=3\times10^{-4}$, $Pr=1$ and $Pm=5$, respectively. No hyperdiffusivities are used in these full-sphere calculations.

All the runs are initialized to zero velocity field and a radial conductive temperature gradient ($l=0$, $m=0$) with random thermal noise imposed as a perturbation. A seed magnetic field, containing both poloidal and toroidal components, initializes each case. The non-dimensional amplitude of the seed field is $|\mathbf{B}|=\Lambda^{1/2}=0.5$. The poloidal part is an axial dipole field (with spherical harmonic degree $l=1$, $m=0$) produced by a radially uniform azimuthal current density distribution. The toroidal part is antisymmetric across the equator ($l=2$, $m=0$) and varies radially such that it is continuous across r_i and vanishes on the outer shell boundary as well as at the origin.

The initial field can affect the final form of the solution. We have carried out additional cases (not presented here) in which we vary the morphology and strength of the seed field and find that strong initial fields facilitate the onset of dynamo action. Thus, to obtain the minimum possible supercritical Rayleigh number for the existence of strong field (i.e., $\Lambda\sim1$) dynamo action, a strong initial field is imposed. Typically, we find strong field dynamos at Ra relatively near Ra_c that have nearly axial dipolar field morphologies, in basic agreement with Aubert and Wicht [25].

Several sets of calculations are performed using different numerical grids in the radial r, latitudinal θ and azimuthal ϕ directions. The number of radial grid points, n_{ro}, are chosen such that there are at least 4 grid points within the Ekman boundary layer, defined as $\delta E=DE^{1/2}$. Since the shell thickness is set to $D=1$ in each calculation, the Ekman layer thickness is independent of the radius ratio. Thus, the number of radial grid levels is fixed at $n_{ro}=41$, which produces the desired radial resolution. The number of grid points in the longitudinal direction, n_ϕ, is chosen so that a grid cell in the middle of an equatorial slice is approximately square. The number of grid points in the latitudinal direction, n_θ, is always chosen to be half those in the longitudinal direction. Therefore, as the radius ratio is increased, finer grids are needed in the longitudinal and latitudinal directions, with maximum spherical harmonic degree l_{max} up to 128. The grid parameters for calculations at each value of χ are given in Table 1.

Table 1
Grid parameters used in the calculations performed in this study at $E=3\times10^{-4}$, $Pr=1$ and $Pm=5$

Radius ratio	$E=3\times10^{-4}$ grid parameters				
χ	n_{ro}	n_θ	n_ϕ	n_{ri}	l_{max}
0.15	41	80	160	17	53
0.25	41	80	160	17	53
0.35	41	80	160	17	53
0.45	41	128	256	25	85
0.55	41	144	288	25	96
0.65	41	192	384	25	128

The first column shows the shell radius ratio, χ. The following columns respectively show the number of shell grid points in radius r, colatitude θ and longitude ϕ, the radial grid points interior to the inner shell and the maximum spherical harmonic degree.

For each χ, a value of Ra is chosen relatively close to Ra_c, the critical value for the onset of non-magnetic rotating convection. See Table 2 for the list of Ra values calculated. If conditions are not favorable for sustaining dynamo action, the magnetic energy in the conducting fluid decays with time, as in the $\chi=0.55$, $Ra=1.5\ Ra_c$ case shown in Fig. 1a. If the magnetic energy drops by three orders of magnitude, the run is labeled a failed dynamo. The run is then repeated with higher values of Ra until self-sustaining, supercritical dynamo action is achieved, as shown in Fig. 1. To be considered a dynamo, the magnetic energy must obtain a statistically steady state. This typically occurs within less than half a magnetic diffusion time, τ_η, which varies with the viscous diffusion time as $\tau_\eta=\tau_v\ Pm/(1-\chi)^2$. As an example, for the $\chi=0.55$, $Ra=2.0\ Ra_c$ case $\tau_\eta=24.7\ \tau_v$ and the magnetic field becomes statistically steady after about 4 τ_v, which is equivalent to 0.16 τ_η.

Table 2
Characteristics of the full-sphere calculations performed in this study at $E=3\times10^{-4}$, $Pr=1$ and $Pm=5$

Radius ratio		Rayleigh number		Calculation time	
	χ	$Ra/10^6$	Ra/Ra_c	τ_v	τ_η
	0.15	0.64	2.0	4.8	0.69
	0.15	0.96	3.0	10.7	1.55
	0.15	1.28	4.0	3.7	0.53
	0.15	1.60	5.0	2.8	0.41
	0.15	1.91	6.0	3.6	0.52
+	0.15	2.23	7.0	32.7	4.74
★	**0.15**	**2.55**	**8.0**	**14.7**	**2.13**
#★	**0.15**	**2.87**	**9.0**	**8.6**	**1.25**
★	**0.15**	**3.19**	**10.0**	**8.5**	**1.23**
	0.25	0.73	3.0	7.7	0.86
	0.25	0.98	4.0	.5	0.73
★	**0.25**	**1.10**	**4.5**	**19.9**	**2.23**
# ★	**0.25**	**1.22**	**5.0**	**9.8**	**1.1**
	0.35	0.42	2.1	7.4	0.63
	0.35	0.50	2.5	10.0	0.85
★	**0.35**	**0.60**	**3.0**	**30.1**	**2.56**
# ★	**0.35**	**0.73**	**3.6**	**35.4**	**3.01**
	0.45	0.35	2.0	9.0	0.54
O ★	**0.45**	**0.41**	**2.3**	**9.2**	**0.55**
# ★	**0.45**	**0.45**	**2.5**	**7.4**	**0.45**
★	**0.45**	**0.52**	**2.9**	**9.8**	**0.59**
	0.55	0.23	1.5	10.2	0.41
	0.55	0.29	1.8	5.9	0.24
O ★	**0.55**	**0.31**	**2.0**	**9.8**	**0.40**
# ★	**0.55**	**0.34**	**2.2**	**8.6**	**0.35**
★	**0.55**	**0.38**	**2.5**	**10.0**	**0.41**
★	**0.55**	**0.46**	**3.0**	**9.8**	**0.40**
	0.65	0.21	1.5	18.3	0.45
★	**0.65**	**0.24**	**1.7**	**21.3**	**0.52**
# ★	**0.65**	**0.28**	**2.0**	**9.3**	**0.23**

The 1st column shows the radius ratio of the fluid shell, while the 2nd and 3rd columns show respectively the Rayleigh number used and its supercriticality. The 4th and 5th columns show the calculation time measured in units of viscous and magnetic diffusion time, respectively. Bold rows with ★ symbols are dynamo cases; others represent failed dynamos. The special case of $\chi=0.15$ and $Ra/Ra_c=7$ (marked by a +) is discussed in the text. Rows marked by a O are quasi-steady dynamos. Rows marked with # symbols represent the fully developed, unsteady dynamo cases with Ra nearest Ra_c. These #-cases are used in Figs. 3 and 4.

In subsequent tables and figures, error bars represent the standard deviations of the relevant quantities averaged over at least one viscous diffusion timescale near the end of each simulation. Additionally, the kinetic and magnetic energy spectra are monitored during each calculation. The power in adequately resolved calculations is required to drop by at least two orders of magnitude from the maximum value in each kinetic and magnetic energy spectrum.

In Table 2 quasi-steady dynamo cases are marked by a O. Weakly supercritical dynamo action is quasi-steady, barring longitudinal drift, and produces a relatively weak magnetic field for radius ratios $\chi=0.45$ and $\chi=0.55$. Kinetic and magnetic energy time series for the quasi-steady $\chi=0.55$ case are shown in Fig. 1. The cases are likely due to the fact that well-organized, quasi-steady columnar convection efficiently generates dynamo action at low degrees of supercriticality in thinner shells. (However, we note that we did not find a quasi-steady dynamo for $\chi=0.65$.) In contrast, lower χ dynamos have vigorous, chaotic flow near dynamo onset due to the relatively high values of Ra/Ra_c.

The case marked by the + in Table 2 corresponds to $\chi=0.15$ and $Ra/Ra_c=7$. This case is special in that, after integrating for 4.74 magnetic diffusion timescales, the weak but strongly fluctuating magnetic field has not decayed but also has not reached a statistical steady state. This case seems to be very close to the critical point of dynamo onset.

In general, increasing Ra just after the onset of dynamo action leads to an increase in the strength and time variation of the magnetic field. For yet higher Ra values the magnetic field strength typically levels off; these cases are referred to here as fully developed dynamos. The fully developed dynamo cases with Ra nearest Ra_c are marked by a # in Table 2. These

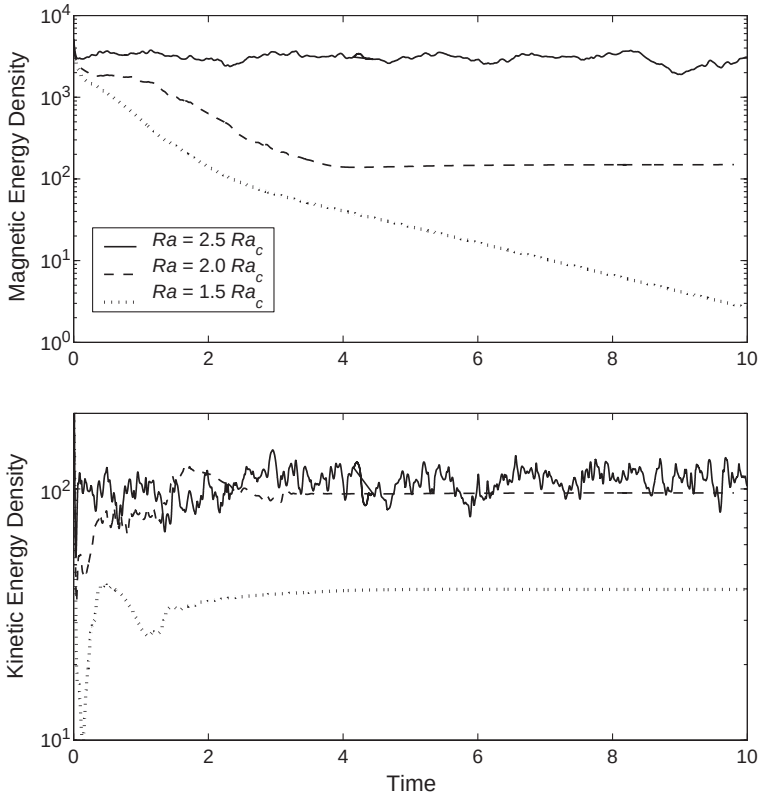

Fig. 1. Time series of the magnetic energy density (top) and kinetic energy density (bottom) for $\chi = 0.55$. Dimensionless time is scaled by the viscous diffusion timescale. Three cases are shown: $Ra = 1.5 \times Ra_c$ is a subcritical case (dotted line); $Ra = 2.0 \times Ra_c$ is a marginally supercritical, steady dynamo case (dashed line); $Ra = 2.5 \times Ra_c$ is a typical dynamo case (solid line).

cases are used in subsequent figures and discussion of dynamo characteristics as a function of radius ratio.

3. Results

Fig. 2a shows failed and successful dynamo solutions. Solid circles mark the successful cases while open circles mark failed dynamos (i.e., non-magnetic solutions). The lowermost, thin solid curve represents the critical Rayleigh number for rotating convection Ra_c, which is given by

$$Ra_c = E^{-\gamma}\left[\frac{C_1}{\chi^2} + C_2\left(\frac{1-\chi}{1+\chi}\right)^{1/2}\right], \qquad (11)$$

where

$$\gamma = 1.16, \quad C_1 = 0.21, \quad C_2 = 22.4,$$
$$\text{and } E = 3 \times 10^{-4} \qquad (12)$$

[30]. The dashed lines represent 2 Ra_c, 3 Ra_c and so on. For each χ value, Ra_d denotes the minimum Ra where a dynamo solution is obtained and these values are fit by the thicker solid line. The ratio Ra_d/Ra_c, which represents the supercriticality of convection at the onset of dynamo action, is inversely proportional to χ, as shown in Fig. 2b. In particular, a large decrease in Ra_d/Ra_c occurs between $\chi = 0.15$ and $\chi = 0.25$.

Fig. 3a shows the kinetic and magnetic energy densities as a function of χ for the lowest Ra fully developed dynamo cases given in Table 2. The kinetic energy densities decrease monotonically with increasing χ. This occurs because Ra_d/Ra_c is decreasing with χ, and nearly levels out for $\chi \geq 0.45$. The magnetic energy density is small for the $\chi = 0.15$ case and peaks at $\chi = 0.45$. This peak may be related to a peak in the volume fraction of core fluid occupied by convection columns, which also occurs near $\chi = 0.45$. Only at $\chi = 0.15$ does the magnetic energy

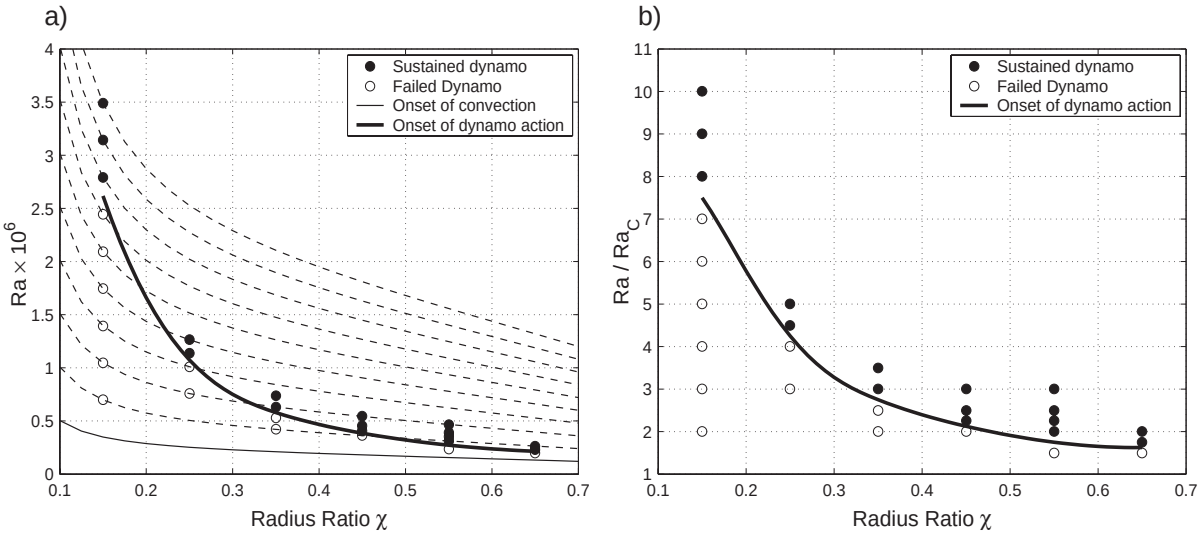

Fig. 2. Regime diagrams in terms of (a) the Rayleigh number Ra and (b) the supercriticality of rotating convection Ra/Ra_c. Both plots show non-magnetic solutions (open circles) and dynamo solutions (closed circles) as a function of χ. Heavy solid lines indicate the onset of dynamo action. Light solid lines show the critical Rayleigh number for rotating convection Ra_c. Dashed lines show integer multiples of Ra_c.

density drop below the kinetic energy density. We note that the kinetic to magnetic energy ratio is expected to be sensitive to our choice of the model parameters (especially Pm). Nevertheless, the trend with χ may be relatively parameter independent. The peak in magnetic energy may be compared to the results of Morrison and Fearn [20]. They obtained a magnetic energy peak at $\chi = 0.25$. Our results seem to be in basic agreement with theirs, considering that they covered a different range of χ-values ($0.025 < \chi < 0.50$), used a different thermal forcing, and scaled the Ekman number differently.

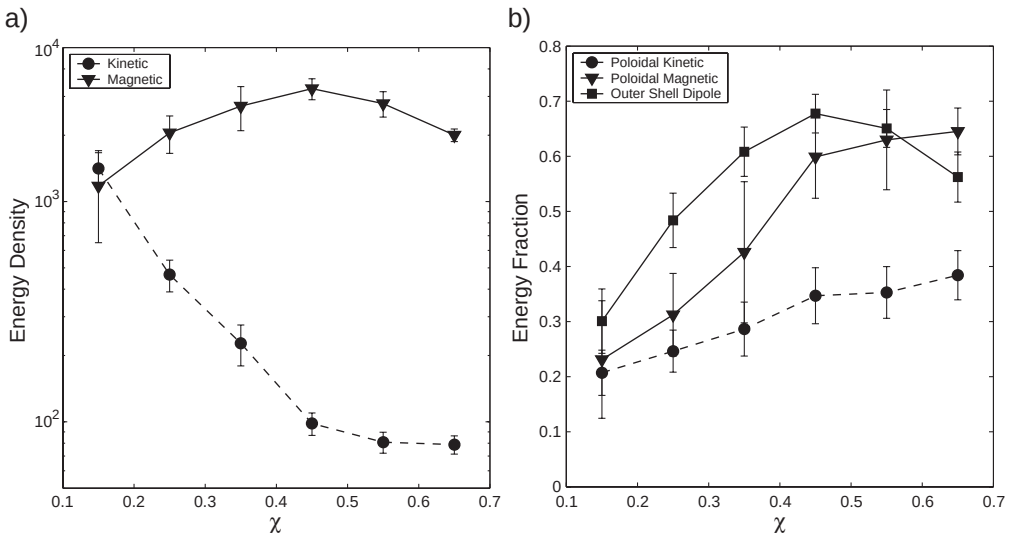

Fig. 3. Energy characteristics as a function of radius ratio χ for fully developed dynamos near the onset of dynamo action (marked by # in Table 2): (a) fluid shell energy density; (b) ratios of poloidal to total kinetic energy, poloidal to total magnetic energy and dipolar to total magnetic energy on r_o.

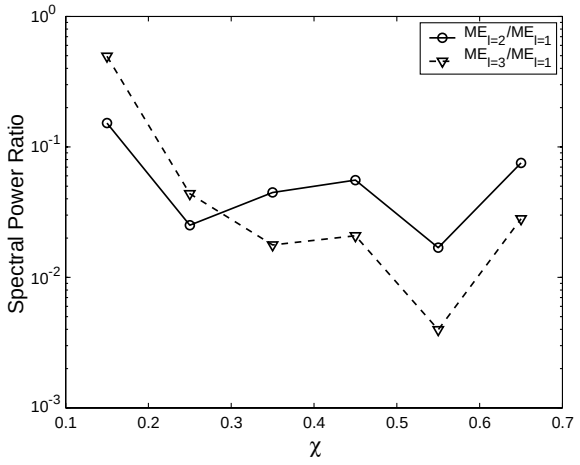

Fig. 4. Ratio of the magnetic spectral power of the quadrupole and dipole components (triangles and dashed line) and the octopole and dipole components for fully developed dynamos near the onset of dynamo action (marked by # in Table 2).

Fig. 3b shows the poloidal kinetic energy fraction and the poloidal magnetic energy fraction averaged over the fluid shell. In addition, the dipole magnetic energy fraction on r_o is displayed. Note in Fig. 3b that the poloidal kinetic energy fraction increases with χ. This differs from the trend for the kinetic energy density shown in Fig. 3a. Thus, a higher percentage of the kinetic energy is contained in poloidal motions in higher radius ratio cases. In our simulations, much of the poloidal kinetic energy is contained in axial flow along convection columns. The axial flow produces fluid helicity, which is diagnostic of poloidal magnetic field generation. Such poloidal motions are secondary to the primary geostrophic flow, and may be driven by a variety of sources, including Ekman pumping in the viscous boundary layer and heterogeneity of thermal buoyancy along convection columns [8].

Fig. 4 shows the ratio of the quadrupole to dipole magnetic field components and the octopole to dipole magnetic field components as a function of radius ratio. The quadrupole–dipole ratio drops by approximately one order of magnitude over the range of χ investigated. The octopole to dipole ratio varies by over two orders of magnitude. Both ratios show a minimum at $\chi=0.55$. Thus, relative to the quadrupole and octopole energies, the dipole energy is at a maximum at $\chi=0.55$.

Table 3 contains a variety of diagnostics from the calculations. In addition to the kinetic and magnetic energy densities of the working fluid, KE and ME, this table contains the magnetic energy density within r_i, ME_{ri}, the magnetic dipole energy fraction, MDE,

Table 3
Time-averaged diagnostics as a function of radius ratio (χ) and Rayleigh number (Ra/Ra_c) for dynamo solutions

χ	Ra/Ra_c	KE	ME	ME_{ri}	MDE	MDE_{ro}	θ_{dip}	ME_{IC}/ME_T
0.15	8.00	1307 ± 190	536 ± 229	358 ± 262	0.04 ± 0.01	0.35 ± 0.07	171 ± 5	0.002 ± 0.001
0.15	9.00	1523 ± 180	1239 ± 326	1155 ± 527	0.03 ± 0.01	0.27 ± 0.04	171 ± 4	0.003 ± 0.001
0.15	0.00	1559 ± 324	1431 ± 392	1588 ± 738	0.04 ± 0.01	0.28 ± 0.06	174 ± 4	0.004 ± 0.002
0.25	4.50	413 ± 62	1515 ± 378	781 ± 346	0.09 ± 0.01	0.57 ± 0.06	174 ± 3	0.008 ± 0.003
0.25	5.00	468 ± 77	2080 ± 390	1065 ± 506	0.10 ± 0.02	0.56 ± 0.06	175 ± 3	0.008 ± 0.003
0.35	3.00	242 ± 36	601 ± 206	163 ± 71	0.10 ± 0.03	0.68 ± 0.05	180 ± 0	0.012 ± 0.003
0.35	3.50	217 ± 37	2824 ± 556	1507 ± 646	0.21 ± 0.03	0.68 ± 0.05	174 ± 3	0.023 ± 0.007
0.45	2.25	120 ± 13	152 ± 4	102 ± 18	0.25 ± 0.05	0.87 ± 0.04	180 ± 0	0.067 ± 0.010
0.45	2.50	98 ± 12	3253 ± 354	2977 ± 293	0.38 ± 0.02	0.74 ± 0.03	177 ± 1	0.092 ± 0.011
0.45	3.00	131 ± 14	3215 ± 301	2562 ± 289	0.33 ± 0.02	0.71 ± 0.03	174 ± 3	0.080 ± 0.011
0.55	2.00	96 ± 0	148 ± 2	106 ± 1	0.37 ± 0	0.89 ± 0	180 ± 0	0.143 ± 0.002
0.55	2.25	81 ± 9	2853 ± 339	2683 ± 274	0.41 ± 0.02	0.75 ± 0.04	178 ± 1	0.190 ± 0.026
0.55	2.50	108 ± 11	3002 ± 377	2605 ± 297	0.37 ± 0.02	0.72 ± 0.04	177 ± 1	0.176 ± 0.033
0.55	3.00	155 ± 15	3300 ± 271	2301 ± 182	0.28 ± 0.01	0.66 ± 0.03	177 ± 2	0.140 ± 0.015
0.65	1.75	62 ± 3	279 ± 26	244 ± 29	0.45 ± 0.02	0.82 ± 0.01	179 ± 0	0.331 ± 0.019
0.65	2.00	79 ± 7	2048 ± 154	1853 ± 242	0.38 ± 0.02	0.73 ± 0.04	179 ± 0	0.342 ± 0.031

Columns three through eight show the kinetic energy density in the fluid shell (KE), magnetic energy density in the fluid shell (ME), magnetic energy in the solid inner conducting volume (ME_{ri}), magnetic dipole energy fraction in the shell (MDE), and on the outer boundary (MDE_{ro}), colatitude of the magnetic dipole axis on the outer boundary (θ_{dip}), and the ratio of inner conducting volume magnetic energy to the total magnetic energy (ME_{IC}/ME_T).

the dipole energy fraction on the outer boundary, MD_{ro}, the colatitude of the average dipole field axis, θ_{dip} and the inner core magnetic energy fraction, ME_{IC}/ME_T. The average value of each quantity is given along with its temporal standard deviation.

Figs. 5 and 6 show images of the flow and magnetic field patterns in the cases studied here. Fig. 5 shows equatorial slices of the temperature field, spherical surface images of radial velocity at mid shell and the radial magnetic field contours on r_o. Panel 5a shows results from the $\chi=0.15$, $Ra/Ra_c=8.0$ case. One turbulent plume occurs in this thick-shelled case. The plume is strongly sheared in the retrograde direction by the zonal flow that exists outside the tangent cylinder (i.e., the imaginary right cylinder parallel to the axis of rotation and circumscribing the inner core equator). Because the intersection of the tangent cylinder with the outer shell radius occurs at high latitude for small χ, the single strong poloidal magnetic field flux bundle is also located at high latitude. Thus the time-averaged magnetic field on the outer boundary is roughly axial.

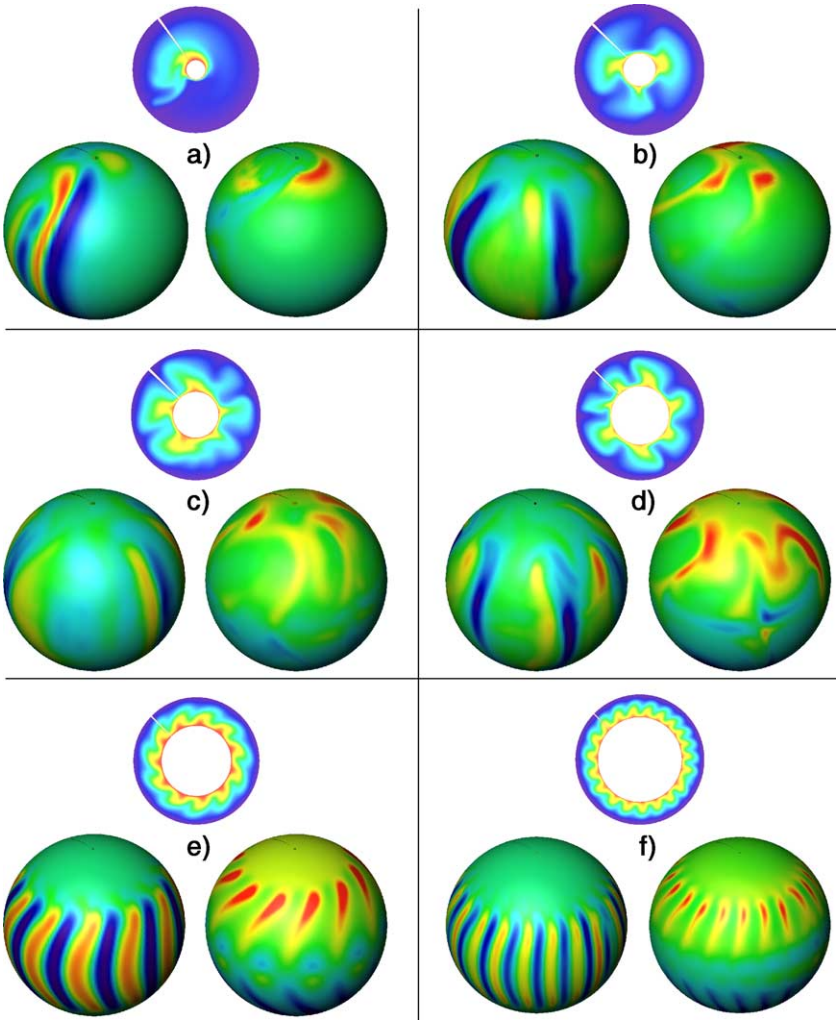

Fig. 5. Images showing the temperature field in the equatorial plane (top), radial velocity at mid shell (left), and radial magnetic field on the outer boundary (right). (a) $\chi=0.15$, $Ra=8\ Ra_c$; (b) $\chi=0.25$, $Ra=4.5\ Ra_c$; (c) $\chi=0.35$, $Ra=3.5\ Ra_c$; (d) $\chi=0.45$, $Ra=3\ Ra_c$; (e) $\chi=0.55$, $Ra=2\ Ra_c$; (f) $\chi=0.65$, $Ra=2\ Ra_c$. $E=3\times10^{-4}$ in all cases. Blue (red) indicates low (high) temperature and high inward (outward) velocity and magnetic field. (For interpretation of the references to colour in this figure legend, the reader is referred to the web version of this article.)

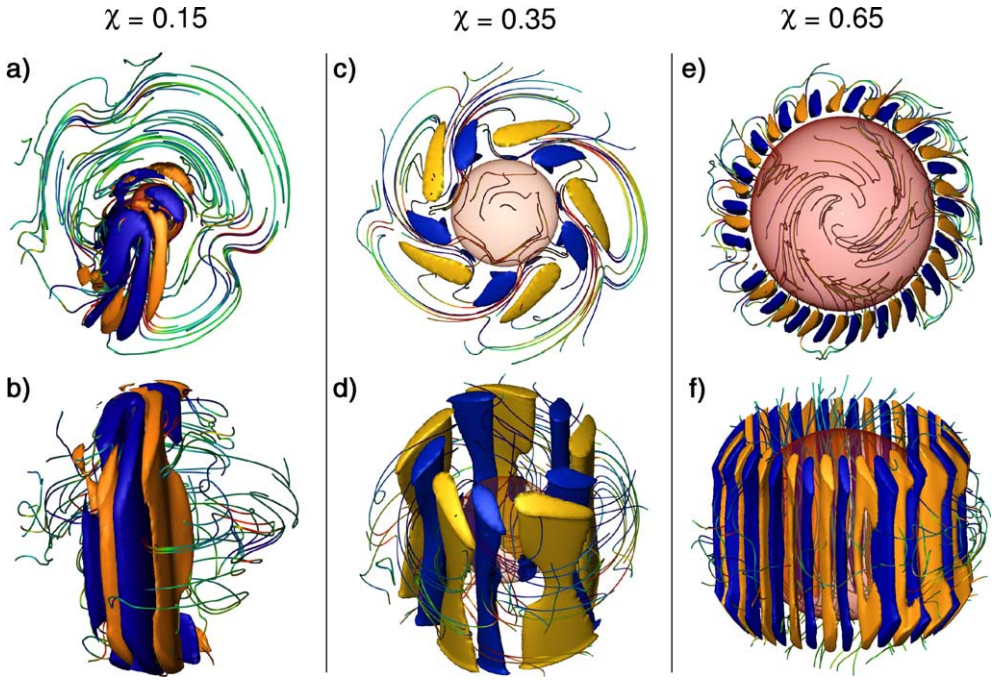

Fig. 6. Axial vorticity and magnetic field lines for the cases shown in Fig. 5. Polar views in the top row and perspective views in the bottom row. Prograde vorticity is represented by orange and yellow isosurfaces, retrograde vorticity by blue isosurfaces. Magnetic field lines are colored according to the relative strength of the radial component such that red and blue indicate outward and inward magnetic flux, respectively. Translucent red spheres indicate the inner shell boundary. The thick shell case (a and b) with $\chi=0.15$ and $Ra=8\ Ra_c$, shows a pair of vorticity isosurfaces associated with a single convective plume. The magnetic field is seen to be mostly toroidal in the region of return flow, which lacks a plume. Poloidal field generation occurs within the vortices (see text for details). Onset of dynamo action occurs at significantly lower Ra/Ra_c for thinner shell cases. For the $\chi=0.35$ case (c and d), dynamo onset is at $Ra=3\times Ra_c$ and for $\chi=0.65$ (e and f) $Ra=1.7\times Ra_c$. (For interpretation of the references to colour in this figure legend, the reader is referred to the web version of this article.)

Panels 5b through 5f show that the number of columnar plumes arrayed just outside the tangent cylinder is proportional to the radius ratio. Dynamo action occurs closer to the critical Rayleigh number as the radius ratio increases. The images in Fig. 6 show axial vorticity surfaces and magnetic field lines. Comparing Figs. 5 and 6, note that the magnetic flux bundles on r_o are associated with the prograde (cyclonic) vortices, in agreement with previous simulations of α^2-dynamos (e.g., [8,25]). In the well-organized, high χ cases, the magnetic field diffuses into the large conducting solid inner core region ($r<r_i$). The large inner core in these cases acts to smooth the field in both space and time. Thus, increasingly strong axial dipole fields are produced in the high χ cases, as is evident in Figs. 5f and 6f.

4. Discussion

4.1. Rayleigh number for variable spherical gap width

Up to this point we have used the standard Rayleigh number Ra based on shell gap thickness D given by Eq. (5). However, for the case of a planet with fixed core radius and a growing inner core, it is appropriate to study convective onset where r_o is held fixed while χ and D vary. In this case we may rewrite Ra using $D=r_o(1-\chi)$ as:

$$Ra(\chi) = Ra^{pl}(1-\chi)^3 \tag{13}$$

$$Ra^{pl} = \frac{\alpha g_o \Delta T r_o^3}{\kappa \nu}. \tag{14}$$

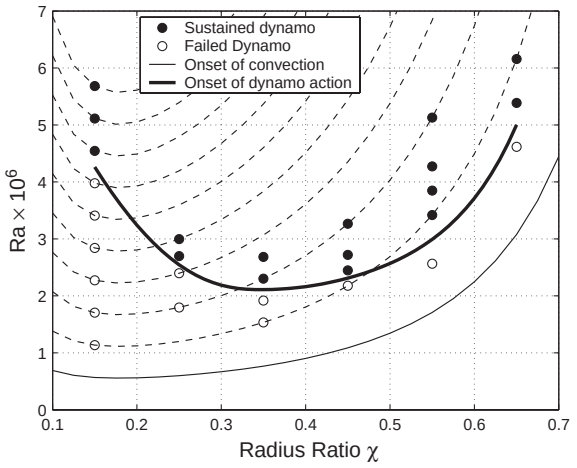

Fig. 7. Regime diagram for the planetary Rayleigh number Ra^{pl} (χ), defined in Eq. (13). Description of symbols and lines is similar to Fig. 2a.

This modified Rayleigh number Ra^{pl}, is referred to here as the "planetary Rayleigh number".

Fig. 7 shows Ra^{pl} as a function of χ for failed and sustained dynamo calculations. The figure is similar to Fig. 2a with Ra^{pl} replacing Ra. Thus, whereas Fig. 2a gives the Rayleigh number in terms of a constant spherical shell gap width D, Fig. 7 gives the same results but with the Rayleigh number rescaled by assuming the outer shell radius r_o is constant. In this representation, the onset of dynamo action has a minimum Ra^{pl} value near $\chi \sim 0.35$. However, it should be noted that the critical planetary Rayleigh number for dynamo action does not vary by more than a factor of 3 over the range $0.15 \leq \chi \leq 0.65$.

4.2. Comparison of thick and thin shell cases

Rotating convection and dynamo generation processes vary significantly with shell geometry. For isothermal boundary conditions, convective plumes originate on the inner shell boundary and a pair of counter-rotating columnar vortices is associated with each thermal plume. The number of columnar plumes is proportional to the radius ratio, as shown in Figs. 5 and 6 as well as in Al-Shamali et al. [30] for non-magnetic rotating convection. Thus, thicker shelled models (with low radius ratios) have fewer convection columns than thinner shelled models.

In the thick shell case with $\chi = 0.15$, convection and dynamo action are driven by upwelling from a single localized region of the inner boundary. In contrast, multiple plumes produce convection columns that surround the inner boundary for cases with $\chi \geq 0.25$. The transition from single plume to multiple plume dynamos is associated with the following major changes in the dynamo characteristics: (1) an abrupt decrease in Ra_d/Ra_c from $\chi = 0.15$ to $\chi = 0.25$. (2) A reversal in the ratio of magnetic to kinetic energy; kinetic energy is greater than the magnetic energy in the single plume cases, whereas the magnetic energy is greater than the kinetic energy for multiple plume dynamos. (3) A strong increase in the dipole magnetic energy relative to the total magnetic energy at the outer boundary in cases with $0.15 \leq \chi \leq 0.45$.

For the $\chi = 0.15$ case, the poloidal field is still produced by the helical flow within a single turbulent convection column. However, the toroidal field is generated mainly by large-scale azimuthal shearing, the so-called ω-effect. Thus, dynamo action in the thick shell case is likely generated predominantly by an αω-dynamo mechanism. To illustrate this, Fig. 8 shows magnetic field lines and an isothermal surface for $\chi = 0.15$. The magnetic field lines are dominantly toroidal outside the convective plume region and are deflected into a poloidal morphology by axial flow associated with the plume structure. The dominantly toroidal field away from the main

Fig. 8. Temperature isosurface and magnetic field lines for the $\chi = 0.15$, $Ra = 8\ Ra_c$ case. The magnetic field lines are colored according to the relative strength of the radial component such that red and blue indicate outward and inward magnetic flux respectively. (For interpretation of the references to colour in this figure legend, the reader is referred to the web version of this article.)

convective plume for $\chi=0.15$ can also be seen in the left column of Fig. 7.

Our model produces relatively strong variations in flow and detailed magnetic field morphology as a function of χ. An interesting feature of the results is a large-scale regionally localized convective structure at $\chi=0.15$. We can compare these results to those of previous studies on the effect of radius ratio on dynamo action. Some of our results are comparable to those of Morrison and Fearn [20]. Although there are several differences in their model formulation from ours, the most significant is the difference in thermal boundary conditions. We have used constant temperature boundary conditions for all of our cases, whereas Morrison and Fearn [20] used pure internal heating. Their model results differ from ours most significantly at $\chi=0.15$. In their model buoyancy production occurs at the outer boundary whereas in ours a strong plume rises from the inner boundary. Furthermore, the dependence of changing χ on their flow and magnetic fields is relatively minor, whereas χ strongly affects our results.

Our results are more similar to those of Roberts and Glatzmaier [21]. They found, as did we, that strong flow and magnetic field structures are located in proximity to the inner boundary tangent cylinder. Their low radius ratio case features flow structures extending from the inner to the outer boundary, comparable in cross section to our regional plume $\chi=0.15$ case. However, unlike our results, their flow and magnetic fields have sources near the outer as well as the inner boundary. This difference in results is likely due mainly to two differences in the model formulation. First, Roberts and Glatzmaier [21] used a combination of buoyancy sources, including both secular cooling effects as well as ICB buoyancy production — the effect of secular cooling explains the relatively strong convection sources near the outer boundary. Second, our lowest radius ratio $\chi=0.15$ is significantly larger than that of their small inner core case ($\chi=0.0875$).

Aubert and Wicht [25] also presented models with a range of relatively large radius ratios ($0.45\leq\chi\leq0.70$). They used a large magnetic Prandtl number ($Pm=14.3$) and obtained equatorial dipole dynamos at Ra very near Ra_c, and axial dipoles at higher Ra/Ra_c. We do not find equatorial dipoles for our models. This is likely due our choice of a lower magnetic Prandtl number ($Pm=5$), so that we first obtain dynamos at higher Ra/Ra_c. This is consistent with the axial dipoles found at similar values of Ra/Ra_c by Aubert and Wicht [25].

4.3. Applications to magnetic field observations

In applying the results of these calculations to planetary dynamos we emphasize that some of parameter values used here are far from those expected for planetary dynamos. For example, despite a variability of 14 orders of magnitude in estimates of the outer core viscosity [38], the Ekman number for the Earth's core is typically estimated as $E\lesssim10^{-12}$. Given that the critical Rayleigh number for rotating convection scales as $E^{-4/3}$, a corresponding estimate for the minimum Rayleigh number in the Earth's core is $Ra\gtrsim10^{16}$. In addition, the magnetic Prandtl number is typically estimated to be less than unity. Thus, by using $E=3\times10^{-4}$, $Ra\sim10^6$ and $Pm=5$, we have placed rather severe restrictions on the parameterization of these dynamo models. Furthermore, as discussed in Section 2.1, we use isothermal boundary conditions and do not model the possible effects of volumetric (radiogenic) heat generation or secular cooling. Nevertheless, previous models with comparably restrictive model parameters have reproduced many of the first order features of Earth's magnetic field (e.g. [34]). While the limitations of the dynamo models presented here must be kept in mind, it seems reasonable to apply our results to observations of magnetic fields of the earth and planets.

In our modeling results axial dipole fields occur over a broad range of radius ratios. Additionally we find that the critical planetary Rayleigh number for dynamo action Ra_d^{pl} varies by less than a factor of three over the range $0.15\leq\chi\leq0.65$, with a minimum Ra_d^{pl} at an "Earth-like" $\chi=0.35$. These findings are consistent with the growing list of solar system bodies that are known to have dynamo-generated axially aligned and dipole-dominant magnetic fields [2].

Table 4 contains Elsasser numbers Λ and Λ_{ro}, averaged over the fluid volume and averaged over the outer boundary, respectively, assuming a fixed outer core radius r_o and variable χ. The values given in Table 4 are calculated from the fully developed dynamo cases marked by a # in Table 2. The

Table 4
Elsasser numbers for different χ with r_o fixed, averaged over the fluid volume (Λ) and averaged over the outer shell surface (Λ_{ro})

χ	Λ	Λ_{ro}
0.15	2.08 ± 0.93	0.010 ± 0.006
0.25	4.10 ± 0.79	0.034 ± 0.009
0.35	6.26 ± 1.42	0.12 ± 0.04
0.45	8.87 ± 0.97	0.37 ± 0.05
0.55	9.28 ± 1.22	0.47 ± 0.06
0.65	8.58 ± 0.56	0.51 ± 0.04

The cases are fully developed dynamos near the onset of dynamo action (marked by # in Table 2).

internal Elsasser numbers, Λ, range roughly from two to ten. Thus, our solutions represent strong field dynamos (in the sense that $\Lambda \gtrsim 1$). In contrast, the outer surface Elsasser number values, Λ_{ro}, are roughly one to two orders of magnitude less than the corresponding Λ values. For the Earth-like χ value of 0.35, we find $\Lambda_{ro}=0.12$, which is not far from the Elsasser number for the geomagnetic field, downward continued to the core–mantle boundary, $\Lambda_{cmb} \simeq 0.3$ [2].

We find that the transition from a single convective plume to multiple plumes (with increasing χ) is accompanied by a decrease in Ra_d/Ra_c, and a strong increase in Elsasser number at the outer shell boundary, Λ_{ro}. The increase in the internal Elsasser number, Λ, is less pronounced than that of Λ_{ro}. Indeed, Λ increases by a factor of less than five over the full range $0.15 \leq \chi \leq 0.65$, whereas Λ_{ro} increases by a factor of fifty. Although our models generate strong internal magnetic fields, the external magnetic fields range from weak for thick shells ($\Lambda_{ro}=0.01$ for $\chi=0.15$) to moderate for thin shells ($\Lambda_{ro}=0.51$ for $\chi=0.65$).

Mariner 10 fly-by data provided an estimated dipole moment of roughly 300 nT R_M^3 for Mercury's magnetic field [39,40]. Thus, this field appears to be weak in the sense that its planetary surface Elsasser number is $\Lambda_{ro} \lesssim 10^{-4}$. Although it is often assumed that Mercury must have a thin shell core geometry, thermal evolution models show that its present core geometry sensitively depends on its mantle convection history and core chemistry [6]. Thus, Mercury may have a sulfur-rich, largely molten core and its weak axially dipolar field may be produced by a localized convection pattern similar to the $\chi=0.15$ single plume case described here. However, for cases with $\chi \geq 0.55$ the magnetic energy density and relative dipole energy both weaken. This suggests that similar thin shell models, existing outside of our present range of investigation, may also generate weak external magnetic fields. Assuming that such thin shell cases exist and differ in detailed field structure on r_o, it may be possible to determine Mercury's core geometry via detailed satellite magnetic field measurements.

Our results may also be applied to the Earth's paleomagnetic field. Here the outer boundary Elsasser number is used as a proxy for relative geomagnetic paleointensity: $\sqrt{\Lambda_{r_o}} \propto |\mathbf{B}|$. For the $\chi=0.15$ the value of Λ_{ro} is an order of magnitude less than that for $\chi=0.35$. This implies that the magnetic paleointensity could increase by a factor of ~3 during the epoch of small inner core radius. Estimation of Archean geomagnetic field intensity is difficult and uncertain [41]. Nevertheless, based on paleointensity measurements on 3.5 Ga Komati Formation lavas, Hale [42] estimated the strength of the Earth's field to have been roughly 1/10 its present-day value. Our results imply that a low intensity paleomagnetic field could have been caused by localized core convection in the presence of a small inner core.

5. Conclusions

We have used numerical models to investigate the transition from non-magnetic rotating convection to self-sustaining dynamo action over the range $0.15 \leq \chi \leq 0.65$, using isothermal boundary conditions, a conducting inner core and strong magnetic field initial conditions. We find that the ratio of the Rayleigh number for the onset of dynamo action and the critical Rayleigh number for rotating convection, Ra_d/Ra_c, varies by a factor of 15 over this range, monotonically decreasing with increasing χ. Thus, dynamo action is generated more efficiently by mildly supercritical rotating convection in a thin shell than in a thick shell. All of the dynamo solutions have an axial dipolar field morphology. For the thickest shell geometry, $\chi=0.15$, a single turbulent plume dynamo is obtained. The strength of the external magnetic field increases with χ. With increasing χ, the larger number of columnar vortices acts to generate more net axial flow, which generates

greater poloidal magnetic field intensity. In addition, the increasing size of the inner conducting volume reinforces the external axisymmetric axial field. Our numerical models result in axial dipole fields occurring over a relatively large range of radius ratios. This is consistent with the predominance of approximately axial dipoles in planetary magnetic field observations. As a planet's solid inner core grows, a transition may occur from regionally localized plume structures to convection that more uniformly fills the fluid outer core. Such a transition could be accompanied by an increase in the external magnetic field. Future studies of low radius ratio dynamo action using different boundary conditions and including the effects of secular cooling, internal heat sources and compositional buoyancy will help constrain the dynamics in this transitional regime.

Acknowledgements

We thank the associate editor and three anonymous referees for helpful comments. This research has been supported by the Natural Sciences and Engineering Research Council (NSERC) of Canada. Support for JA has been provided by NASA Grants NAG5-4077 and NAG5-10165. Computational resources have been provided by the Western Canada Research Grid (WestGrid).

References

[1] M.G. Kivelson, J. Warnecke, L. Bennett, et al., Ganymede's magnetosphere: magnetometer overview, J. Geophys. Res. 103 (1998) 19963–19972.
[2] D.J. Stevenson, Planetary magnetic fields, Earth Planet. Sci. Lett. 208 (2003) 1–11.
[3] J.E.P. Connerney, Magnetic fields of the outer planets, J. Geophys. Res. 98 (1993) 18659–18679.
[4] M.H. Acuña, J.E.P. Connerney, Wasilewski, et al., Magnetic field of Mars: summary of results from the aerobreaking and mapping orbits, J. Geophys. Res. 106 (23) (2001) 403–417.
[5] H. Harder, G. Schubert, Sulfur in Mercury's core? Icarus 151 (2001) 118–122.
[6] S.A. Hauck, A.J. Dombard, R.J. Phillips, S.C. Solomon, Internal and tectonic evolution of Mercury, Earth Planet. Sci. Lett. 222 (2004) 713–728.
[7] G.A. Glatzmaier, P.H. Roberts, A three-dimensional convective dynamo solution with rotating and finitely conducting inner core and mantle, Phys. Earth Planet Inter. 91 (1995) 63–75.
[8] P. Olson, U. Christensen, G.A. Glatzmaier, Numerical modeling of the geodynamo: mechanisms of field generation and equilibration, J. Geophys. Res. 104 (1999) 10383–10404.
[9] N. Ishihara, S. Kida, Dynamo mechanism in a rotating spherical shell: competition between magnetic field and convection vortices, J. Fluid Mech. 465 (2002) 1–32.
[10] H.K. Moffatt, Magnetic Field Generation in Electrically Conducting Fluids, Cambridge University Press, Cambridge, 1978.
[11] W.-J. Kuang, J. Bloxham, An Earth-like numerical dynamo model, Nature 389 (1997) 371–374.
[12] B.A. Buffett, The thermal state of Earth's core, Science 299 (2003) 1675–1677.
[13] S. Labrosse, Thermal and magnetic evolution of the Earth's core, Phys. Earth Planet Inter. 140 (2003) 127–143.
[14] S. Labrosse, J.P. Poirier, J.L. Le Mouel, The age of the inner core, Earth Planet Sci. Lett. 190 (2001) 111–123.
[15] F. Nimmo, G.D. Price, J. Brodholt, D. Gubbins, The influence of potassium on core and geodynamo evolution, Geophys. J. Int. 156 (2004) 363–376.
[16] D. Gubbins, D. Alfe, G. Masters, G.D. Price, M. Gillan, Gross thermodynamics of two-component core convection, Geophys. J. Int. 157 (2004) 1407–1414.
[17] B.A. Buffett, H.E. Huppert, J.R. Lister, A.W. Woods, On the thermal evolution of the Earth's core, J. Geophys. Res. 101 (1996) 7989–8006.
[18] J.R. Lister, B.A. Buffett, The strength and efficiency of thermal and compositional convection in the geodynamo, Phys. Earth Planet Inter. 91 (1995) 17–30.
[19] S.J. Drew, Thermal convection in a spherical shell with a variable radius ratio, Geophys. Astrophys. Fluid Dyn. 59 (1991) 165–183.
[20] G. Morrison, D. Fearn, The influence of Rayleigh number, azimuthal wavenumber and inner core radius on 2.5D hydromagnetic dynamos, Phys. Earth Planet Inter. 117 (2000) 237–258.
[21] P.H. Roberts, G.A. Glatzmaier, The geodynamo, past, present and future, Geophys. Astrophys. Fluid Dyn. 94 (2001) 47–84.
[22] A. Sakuraba, M. Kono, Effect of the inner core on the numerical solution of the magnetohydrodynamic dynamo, Phys. Earth Planet Inter. 111 (2000) 105–121.
[23] G. Schubert, K. Zhang, Effects of an electrically conducting inner core on planetary and stellar dynamos, Astrophys. J. 557 (2001) 930–942.
[24] N. Ishihara, S. Kida, Equatorial magnetic dipole field intensification by convection vortices in a rotating spherical shell, Fluid Dyn. Res. 31 (2002) 253–274.
[25] J. Aubert, J. Wicht, Axial and equatorial dipolar dynamo action in rotating spherical shells, Earth Planet. Sci. Lett. 221 (2004) 409–419.
[26] E. Grote, F. Busse, A. Tilgner, Convection-driven quadrupolar dynamos in rotating spherical shells, Phys. Rev. E. 60 (1999) 5025–5028.
[27] E. Grote, F. Busse, A. Tilgner, Regular and chaotic spherical dynamos, Phys. Earth Planet Inter. 117 (2000) 259–272.

[28] E. Grote, F. Busse, Hemispherical dynamos generated by convection in rotating spherical shells, Phys. Rev. E. 62 (2000) 4457–4460.
[29] S. Stanley, J. Bloxham, Convective-region geometry as the cause of Uranus' and Neptune's unusual magnetic fields, Nature 428 (2004) 151–153.
[30] F. Al-Shamali, M.H. Heimpel, J.M. Aurnou, Varying the spherical shell geometry in rotating thermal convection, Geophys. Astrophys. Fluid Dyn. 98 (2004) 153–169.
[31] C.A. Jones, A.M. Soward, A.I. Mussa, The onset of thermal convection in a rapidly rotating sphere, J. Fluid Mech. 405 (2000) 157–169.
[32] S. Weinstein, P. Olson, Planforms in thermal convection with internal heat sources at large Rayleigh and Prandtl numbers, Geophys. Res. Lett. 17 (1990) 239–242.
[33] M. Kono, P.H. Roberts, Definition of the Rayleigh number for geodynamo simulation, Phys. Earth Planet. Inter. 128 (2001) 13–24.
[34] C. Kutzner, U. Christensen, From stable dipolar towards reversing numerical dynamos, Phys. Earth Planet Inter. 131 (2002) 29–45.
[35] G.A. Glatzmaier, Numerical simulations of stellar convective dynamos: I. The model and the method, J. Comput. Phys. 55 (1984) 461–484.
[36] U.R. Christensen, P. Olson, G. Glatzmaier, Numerical modelling of the geodynamo: a systematic parameter study, Geophys. J. Int. 138 (1999) 393–409.
[37] J. Wicht, Inner-core conductivity in numerical dynamo simulations, Phys. Earth Planet Inter. 132 (2002) 281–302.
[38] R.A. Secco, Viscosity of the outer core, in: T. Ahrens (Ed.), Mineral Physics and Crystallography, American Geophysical Union, 1995.
[39] N.F. Ness, K.W. Behannon, R.P. Lepping, Y.C. Whang, The magnetic field of Mercury, J. Geophys. Res. 80 (1975) 2708–2716.
[40] S.C. Solomon, Mercury: the enigmatic innermost planet, Earth Planet. Sci. Lett. 216 (2003) 441–455.
[41] J-P. Valet, Time variations in geomagnetic intensity, Rev. Geophys. 41 (2003) 1–44.
[42] C.J. Hale, The intensity of the geomagnetic field at 3.5 Ga: paleointensity results from the Komati formation, Barberton Mountain Land, South Africa, Earth Planet. Sci. Lett. 86 (1987) 354–364.
[43] G.A. Glatzmaier, Geodynamo simulations: how realistic are they? Annu. Rev. Earth Planet Sci. 30 (2002) 237–257.